# Long-term stability of the microstructure of austenitic ODS steel rods produced with a carbon-containing process control agent

**Tim Gräning\*, a, Michael Klimenkov[a], Michael Rieth[a], Cornelia Heintze[b], Anton Möslang[a]**

a) Karlsruhe Institute of Technology (KIT), Institute for Applied Materials (IAM), Hermann-von-Helmholtz-Platz 1, 76344 Eggenstein Leopoldshafen, Germany
b) Helmholtz-Zentrum Dresden Rossendorf, Dresden, 01328 Germany

*Corresponding author. Tel +49 721 608 24093; fax: +49 721 608 24567.
E-mail address: tim.graening@kit.edu

## Abstract

Austenitic oxide dispersion strengthened (ODS) steel rods containing a carbon-rich process control agent were annealed at 700, 900 and 1100 °C for up to 1500 hours. An added process control agent was necessary during the process of mechanical alloying to guarantee a reproducible process. In this study, the impact of he added carbon-rich process control agent on the microstructure was determined. For that reason an extruded austenitic ODS steel rod , which designated operation temperature in future power plants is about 700 °C and beyond, was annealed and examined. The investigation revealed, that the microstructure remains stable up to 900 °C. However, a long-term annealing at 1100 °C increased the grain and precipitates size significantly, which resulted in a decline of the mechanical properties. We think, that the amount of carbon and the related formation of carbides has reduced the temperature threshold for coarsening of nano-sized oxide precipitate. The direct impact of carbon on the formation of nano precipitates and their behavior at elevated temperature was shown by calculations of the activation energy of precipitate growth.

## Keywords:

- Austenitic ODS steel
- Process control agent
- Mechanical alloying
- TEM
- EBSD
- Activation energy

## 1. Introduction

Oxide dispersion strengthened (ODS) steels are promising candidates as a structural material for future power plants, due to their ability to maintain their structural integrity at very high temperatures of up to around 80 % of the melting temperature [1]. However, the production process via mechanical alloying is difficult to control, due to its inherent characteristic of being a batch process. Additionally it was shown, that mechanical alloying of ductile powders leads to a decreased production yield, which is caused by an increased tendency of cold welding between the powder particles and the attritor. Research has shown, that it can only be prevented by adding a process control agent (PCA). In a previous publication, the powder of austenitic ODS steel, which was produced with the aid of a carbon-rich PCA, was examined, followed by an investigation of the same material in extruded condition. This research has given rise to questions about an indirect effect of carbon on the microstructure; large carbides were observed and an unexpected growth of precipitates was measured. Even though no change of the orientation relationship between particles and the austenitic matrix was detected and no direct involvement of carbon in the formation of precipitates after an annealing of two hours at temperatures up to 1100 °C was observable, an unprecedented growth of ODS precipitates was recorded. However, recent studies

have revealed that the microstructure of austenitic ODS steel remains stable after an annealing of 100 hours at 1150 °C [1].

To reveal the reason of the above mentioned unexpected growth of precipitates in the previous study, this publication aims to solve the conundrum by applying a systematic approach. Several heat treatments of extruded material were conducted by applying four different annealing times (750, 1000, 1250 and 1500 hours) at 700, 900, and 1100 °C to investigate the impact of carbon on the microstructure. The grain and precipitate sizes were determined and evaluated in respect to the applied annealing temperature. Furthermore, the size distribution and the phase composition of precipitates were identified for all heat treatment conditions and used to calculate the activation energy for grain boundary diffusion and volume diffusion to figure out a possible influence of carbon on the formed microstructure.

## 2.  Material

The mechanical alloying and extrusion process of the material is described elsewhere [QUELLE TIM 2]. The material is labelled as PCA-2 to be consistent with prior publications [QUELLE TIM 1, 2]. For simplicity the actual chemical composition of the extruded rod (Ø 16 mm) is provided once again in **Fehler! Verweisquelle konnte nicht gefunden werden.**. Pieces with a length of around 90 mm were cut off the rod and annealed under ambient atmosphere at 700, 900, and 1100 °C for 750, 1000, 1250, and 1500 hours at each temperature. After the heat treatment, the surface layer was strongly oxidized and was not investigated. Instead, three slices of around 1 mm each were cut from the center of each rod and ground and polished to a thickness of around 200 µm. The final polishing step was performed utilizing a 1 µm diamond polish suspension. As the region of interest, the middle of the sample was chosen assuming, that the oxidation, the diffusion of carbon, and other processes related to the oxidation of the surface area can be neglected. Figure 1 shows the approximate position, where samples have been cut out and also the region of interest (ROI) in the center of the disc highlighted in red. The white arrows are pointing at the ROI and represents the extrusion direction as well as the normal direction of all electron backscatter diffraction (EBSD) and transmission electron microscopy (TEM) maps in this publication. The heat treatment and all applied investigation methods are summarized in **Fehler! Verweisquelle konnte nicht gefunden werden.**. The as-extruded condition of the rod was investigated in the prior study and is used for comparison to the present study [QUELLE TIM 2]. Hereinafter, if specific samples are mentioned, they are referred to as "annealing temperature / annealing time" samples

*Table 1:  Chemical composition of PCA-2 in as-extruded condition*

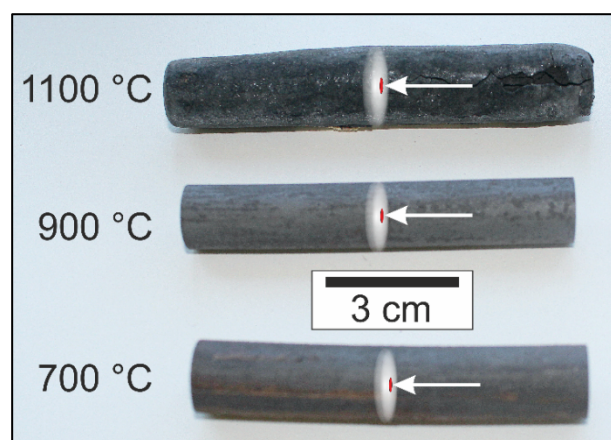| Rod | Fe | Cr | Ni | W | Mn | Ti | V | Y | O | C |
|---|---|---|---|---|---|---|---|---|---|---|
| PCA-2 | 66.6 | 16.0 | 14.1 | 1.52 | 0.37 | 0.16 | 0.16 | 0.18 | 0.14 | 0.28 |



Figure 1:  Pieces of the rod after annealing for 1500 hours under ambient atmosphere. The white discs in the middle of each rod represents the cut out slices. The red area in the middle of the disc was selected as the area of interest for SEM and TEM samples to minimize the influence of the oxidation on the surface of each sample.

*Table 2: Test matrix to determine the grain size with the help of EBSD images and the precipitates size using TEM methods. The as-extruded state was additionally investigated applying atom probe tomography [==PAPER APT TIM==]*

| Annealing time / h | Temperature / °C | | |
|---|---|---|---|
| | 700 | 900 | 1100 |
| 750 | TEM / EBSD | TEM / EBSD | TEM / EBSD |
| 1000 | TEM | TEM | TEM |
| 1250 | TEM | TEM | TEM |
| 1500 | TEM / EBSD | TEM / EBSD | TEM / EBSD |

## 2.1. SEM

The previously mentioned discs were electro-polished for 15 seconds using a mixture of 20% $H_2SO_4$ and 80% $CH_3OH$ as an electrolyte with the purpose to remove the surface area, in which strain and stress was induced during the grinding and polishing process. A final cleaning was done, by rinsing the sample with isopropanol. A Zeiss Merlin field-emission gun scanning electron microscope with GEMINI II electron optics and an acceleration voltage of 20 keV for EBSD was used for investigation. Kikuchi patterns were recorded with an EDAX Hikari high-speed EBSD camera and evaluated by TEAM and OIM Analysis 8.0 software. A minimum confidence index (CI) of 0.1 was applied and misorientation angles higher than 10° were set as grain boundaries. All maps are presented and evaluated in an orthogonal direction with respect to the sample and as shown by the white arrow in Figure 1: Pieces of the rod after annealing for 1500 hours under ambient atmosphere. The white discs in the middle of each rod represents the cut out slices. The red area in the middle of the disc was selected as the area of interest for SEM and TEM samples to minimize the influence of the oxidation on the surface of each sample.Figure 1.

## 2.2. TEM

A small discs with a diameter of 3 mm was punched out of the ROI. Electro-polishing of the punched out disc was carried out in a TENUPOL V device with a mixture of 20% $H_2SO_4$ and 80% $CH_3OH$ as an electrolyte at 20 °C. A final milling was implemented using a precision ion polishing system (PIPS II Model 695 device by GATAN). Shallow angles (4°) and energies ranging between 2 to 0.5 keV were applied to remove possible preparation defects on the sample surface and to enlarge the size of the electron-translucent area for TEM investigations. A FEI Talos F200X microscope equipped with a Super-X-System for energy dispersive x-ray spectroscopy (EDS) was used in combination with a high-visibility-low-background double-tilt holder to obtain a high data acquisition rate. All images were detected by a high angle annular dark field detector and taken in scanning TEM (STEM) mode. Two to three STEM EDS maps were used for each sample condition to determine the mean diameter of precipitates. A 3x3 smooth map filter was applied to all EDS maps.

## 2.3. Hardness tests

Vickers hardness measurements were performed using a load of 0.981 N for all samples. Twelve indentations were taken for each sample in the ROI with a distance of 0.2 mm between each, whereby the minimum and maximum value were considered as outliers. The other ten indentations were used to calculate the average hardness value. The error bars represent the calculated standard deviation around the mean value. The indentation direction was parallel to the extrusion direction (white arrows in Figure 1).

# 3. Results & Discussion

A strong influence of the heat treatment at 1100 °C on the surface of the rod is observable in Figure 1, where a change in volume as well as a formation of cracks on the right side of the rod can be seen. However, this was an expected effect of the annealing under ambient atmosphere. The oxidation is responsible for the change in volume, which induced stress and led to the formation of cracks on the surface. Only a slight influence on the surface for applied temperatures of 700 and 900 °C is visible. By choosing the center of the cross section of the rods as the ROI for the entire investigation, the visible effects on the surface should not have an impact on the

microstructure in the ROI and therefore have not been taken into consideration as an influencing factor on the results of this study.

Figure 1Figure 2 shows inverse pole figure (IPF) maps of the ROI in the as-extruded condition and after an applied annealing at 700, 900, and 1100 °C for 1500 h on the left-hand side. The phenomenon of a smaller grain size after annealing in comparison with the as extruded condition, which is shown in the IPF maps of the samples heat-treated at 700 and 900 °C, is explained elsewhere [Paper-TIM-EXT]. During an annealing at 1100 °C a strong grain growth occurred accompanied by the formation of large $M_{23}C_6$ and Ti-O precipitates. A lot of recrystallization twin boundaries are visible (highlighted in yellow), which let us infer, that a primary and secondary recrystallization occurred. The rate of grain growth $dR/dt$ can be expressed by [2]:

| | | |
|---|---|---|
| *Rate of the grain growth:* | $$\frac{dR}{dt} = M \cdot (P - P_Z)$$ | (1) |
| *Driving force for grain growth* **P**: | $$P = \frac{\alpha \gamma_b}{R}$$ | (2) |
| *Zener pinning pressure* **Pz**: | $$P_Z = \frac{3 f \gamma_b}{2r}$$ | (3) |

where M is the grain boundary mobility, $P$ is the driving force for grain growth, $P_Z$ is the Zener pinning pressure, $\alpha$ is a shape factor, $\gamma_b$ is the boundary energy, $R$ is the sub grain radius, $f$ is the volume fraction of precipitates, and $r$ is the mean radius of precipitates. If the driving force for grain growth is larger than the Zener pinning pressure exerted by the ODS precipitates on the grain boundaries, grain growth occurs. A linear relationship between the size of precipitates and the grain size was found [2]. From equation (3) it can be concluded, that the Zener pinning pressure gets reduced, when the precipitate size increases and/ or the volume fraction decreases. For that reason, the focus of this study was put on the investigation of the growth of precipitates in conjunction with the grain growth and to understand the underlying mechanisms.
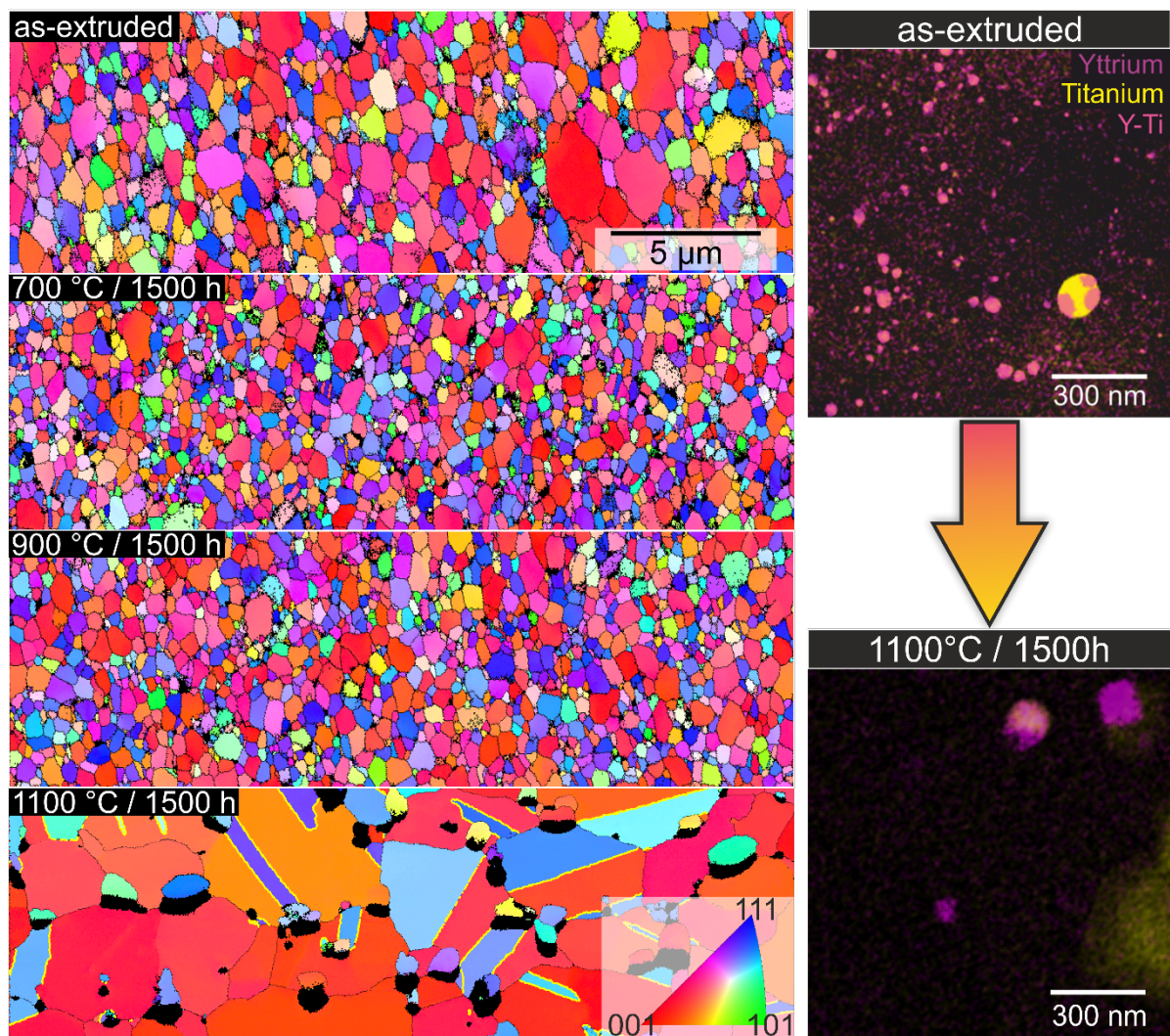
Figure 2: Evolution of the grainsize after a long-time annealing at different temperatures. Yellow lines are representative for annealing twins. Differences in terms of the precipitates for the non-annealed and the 1100 °C / 1500 h sample are shown on the right side.

The right side of Figure 2 features scanning TEM (STEM) EDS maps of yttrium and titanium in as-extruded (top) and "1100 °C / 1500 h" (bottom) condition. In the as-extruded condition, a wide range of precipitate sizes is visible. A large fraction of the precipitates smaller 40 nm in diameter contain both elements: yttrium and titanium. Additional to the small precipitates, on the bottom right side of the image of the as-extruded condition, a larger yttrium-free, titanium-rich precipitate is visible, with a diameter of around 130 nm. Some of the aforementioned smaller yttrium- and titanium-rich precipitates are located adjacent to the large Ti-rich precipitate. The formation of large Ti-O precipitates was mentioned and discussed in recent publications and is common for ODS steels, if the oxygen level is locally increased (>4 at.-%) [3–5]. However, a comparison of the as-extruded and the heat-treated condition reveals a strongly changed microstructure after the heat treatment, which was not yet reported after an annealing at relatively low temperatures of 1100 °C for ODS steels. Additionally, the nano-sized precipitates were tremendously increased in size and decreased in number. The bottom right side of the image "1100 °C / 1500 h" of Figure 2 exhibits a part of a larger titanium-rich and yttrium-free precipitate. Only three large precipitates can be seen in the rest of the investigated area. They are to some extent cubic-shaped, rich in yttrium and partly denuded of titanium. Especially the last-named spatial separation of titanium and yttrium is interesting and unexpected, since the often reported $Y_2Ti_2O_7$ precipitates should be stable in its chemical composition and size at temperatures up to 1200 °C [1,6–8]. The decreased number of precipitates, as well as their growth decrease the Zener pinning pressure (3) and delivers the explanation for the large grain size in "1100 °C / 1500 h". A prior publication has shown, that a short heat treatment of 2 hours at 900 and 1100 °C leads to a slight growth of precipitates, if an abundance of carbon is present in the matrix

material. To understand the influence of a long-term heat treatment on the microstructure, it was necessary to determine the threshold temperature and time, where and when changes in the microstructure are happening. According to Figure 2, this change in the microstructure occurs between 900 and 1100 °C.

To investigate the change in more detail, Figure 3 and Figure 4 present STEM HAADF images with similar magnifications and EDS maps of representative regions of the 900 °C / 1250 h and the 1100 °C / 1500 h samples, respectively. A lot of the bright precipitates (HAADF image) with an average size of 200 to 500 nm shown in Figure 3 have been identified as carbides. They contain mostly Cr, V, W, O, and sometimes Ti. After the formation of these large carbides, several ODS precipitates were found to be similar in size and number to the as-extruded condition (Figure 2, and Ref. [Tim Paper]). However, most of the Y-Ti-O precipitates are located along the grain boundaries (dashed lines) in the 900 °C / 1250 h sample, which proves the successful pinning of the grain boundaries. A correlation of the ODS precipitates and the carbide formation was not observed. The 1100 °C / 1500 h sample, shown in Figure 4, exhibits a completely different microstructure. Strongly increased grains and carbides with a diameter of 1 µm and more were found. Only a few ODS precipitates are detectable, were the small ones are able to pin dislocations. These precipitates are highlighted by white arrows in the HAADF image of Figure 4. This indicates that the remaining small precipitates are able to procrastinate and hinder the migration of dislocations. However, the reduced number and the increased size of precipitates led to a decreased grain boundary pinning force and therefore to a grain growth. An $Y_2O_3$ precipitate adjacent to a larger Ti-Cr-C precipitate is pointed out by a white arrow in the EDS maps in Figure 4, to exhibit one example of the several multiphase clusters, which were found frequently in all samples. A high solubility of oxygen in carbides, i.e. in the M23C6 phase, explains the finding of oxygen in the carbides in the EDS map in Figure 3 and Figure 4 [9].
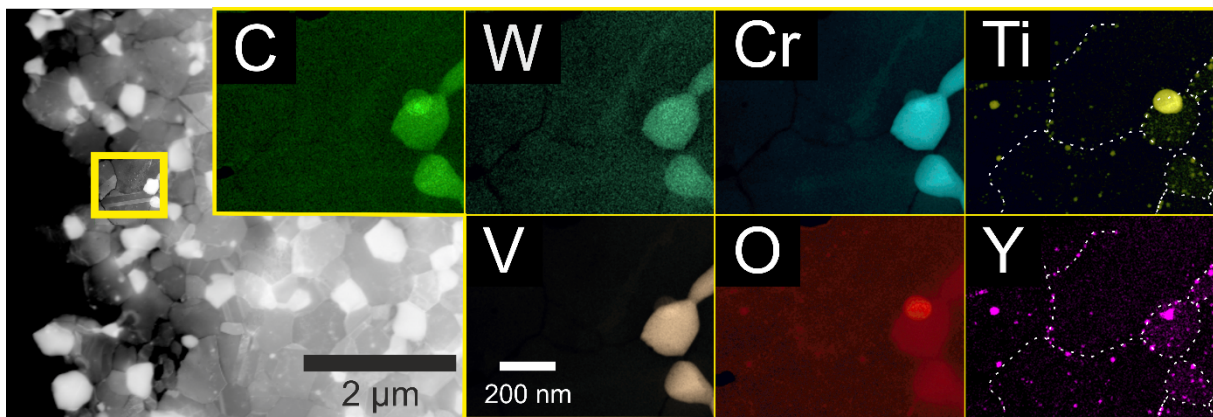


Figure 3:    HAADF image of sample 900 °C / 1250 h next to EDS maps of selected elements. The bright large precipitates (HAADF image on the left) contain mostly Cr, V, W, O, Mn (not shown) and C. The yellow framed region shown in the HAADF image was used for the EDS analyses. White dashed lines represent grain boundaries in the Ti and Y EDS maps.
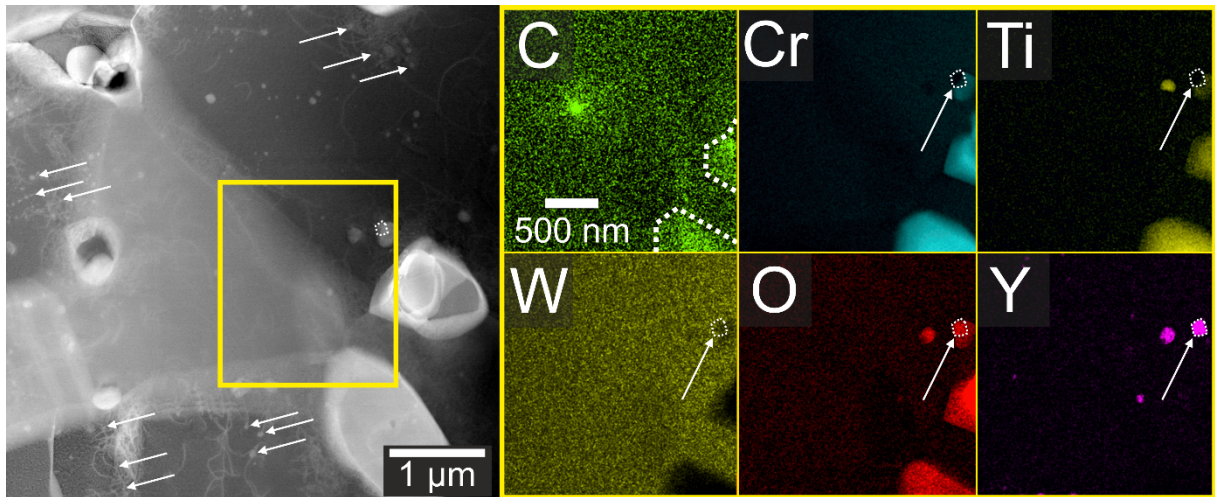
Figure 4:   HAADF image of the annealed rod (1100 °C / 1500 h) on the right side next to EDS maps of the yellow framed area. Mn and V are found in the same location as Cr and have formed carbides. The bright spot in the EDS map of carbon is an artifact. White arrows in the HAADF image show dislocations pinned by precipitates. The white arrow in the EDS maps highlights an yttrium-rich precipitate, devoid of Ti, V, and Cr.

Figure 5 exemplarily shows combined EDS maps of Ti and Y for all conditions (see Table 2:        Test  matrix  to determine the grain size with the help of EBSD images and the precipitates size using TEM methods. The as-extruded state was additionally investigated applying atom probe tomography [PAPER APT TIM]Table 2). Titanium is represented in yellow, yttrium in violet and the Y-Ti precipitates are colored in pink. All maps exhibit the same magnification, except the one shown for the 1100 °C / 1500 h sample. In this case it was necessary to decrease the magnification to record enough of the coarsened precipitates to calculate a reasonable mean diameter.

A careful evaluation of the EDS maps is necessary to minimize possible measuring errors, regarding the size of the particles and their composition. The TEM sample thickness of the measured area plays an important role in the evaluation of the number density of precipitates, due to a rather short extinction length of elements with a small atomic number Z. If the sample is too thick, the x-rays emitted by elements with a small Z will be extinct by the surrounding steel matrix, if the feature is too far away from the surface.  But due to the very same preparation process for all samples and because the scanned area was always set at approximately the same distance from the hole in the sample, it is reasonable to assume, that the influence of the thickness is neglectable. Furthermore, the precipitates where assumed to be of a spherical shape for calculations of the average diameter and standard deviation. The software ImageJ [10] was utilized to generate a binary image, which was then used to calculate the diameter of all precipitates for each sample condition. To do that, a simplified approach was chosen: the measured area for each particle was taken and used to fill the area of a circle, from which the diameter was determined. Upon closer examination of Figure 5, this approach is vindicated by the vast majority of circular features and should result in reasonable and comparable diameter.
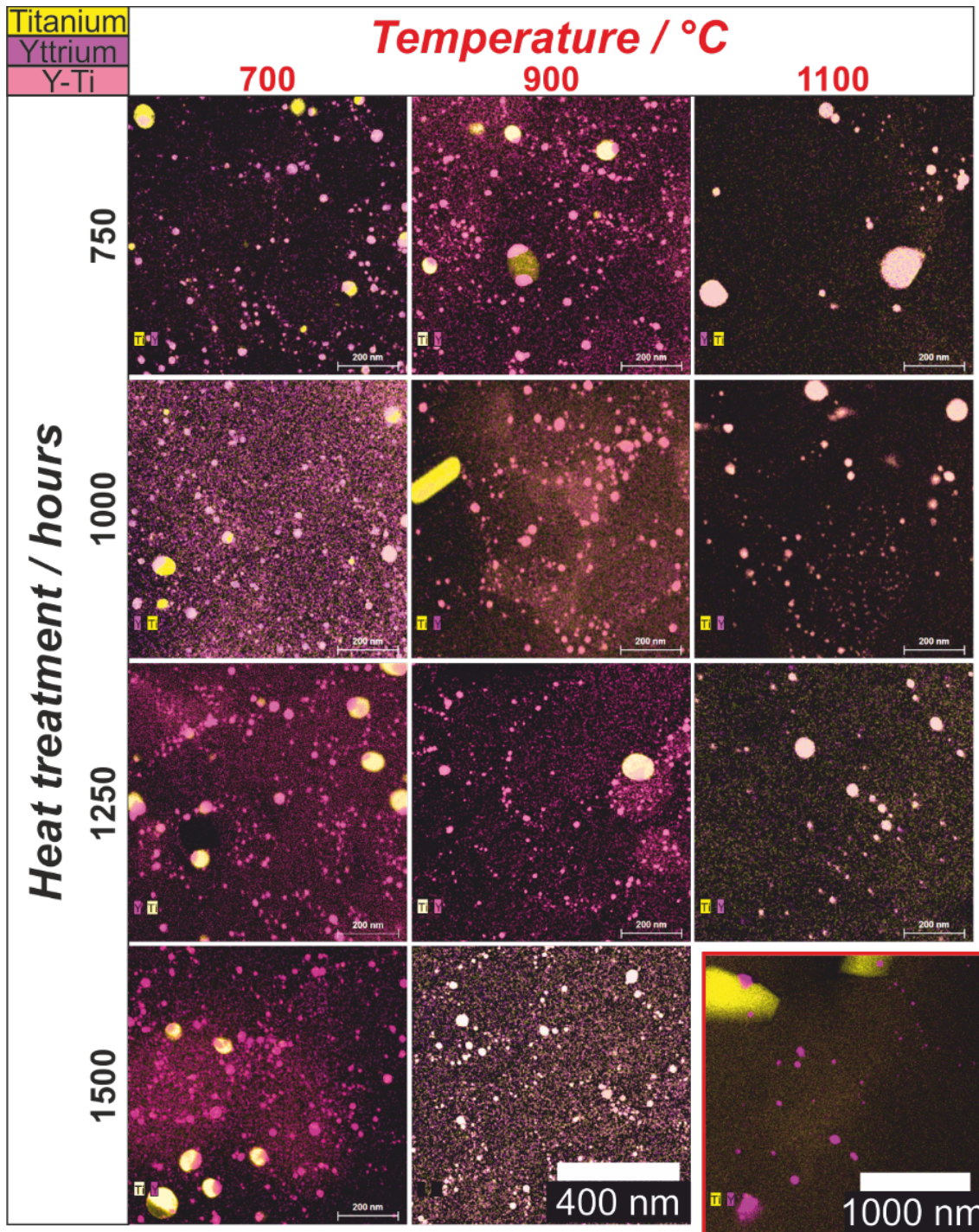
Figure 5: EDS STEM maps of titanium and yttrium for the entire test matrix. All images have the same magnification, except the image of the 1500 h / 1100 °C sample. A lower magnification had to be chosen, after only few precipitates were found (cf. Figure 2)

Evaluating the thermal stability of the precipitates is not only a matter of the size and growth of the precipitates, but also of their chemical composition. For that, due to the abundance of investigated precipitates, a simplified phase analysis was performed, which only distinguishes between yttrium-rich or titanium-rich or yttrium- and titanium-rich precipitates. Here, a detailed analyses of the various possible phases and their dependency on the oxygen content is not part of the discussion and is already presented in prior publications [1,11–14]. The identification of the three different compositions was done by superimposing the element specific EDS maps. A color threshold was chosen to distinguish between the three mentioned compositions and the area phase fractions of the analysis are shown in a normalized block diagram Figure 6. The predominant phase of ODS precipitates in the as-extruded state is a Y-Ti-O phase. Only a very small area fraction of precipitates were found

to be yttrium or titanium-free. It is also worth mentioning, as it was already visible in Figure 4, that titanium was present in carbides and also in oxides. No separation was carried out to distinguish between Ti-O and Ti-C in Figure 6. Despite the high fluctuation in the amount and size of the titanium-rich carbides and oxides in the ROI, a clear change in the area phase fraction of the "1100 °C / 1500h" sample in comparison with all other temperatures is visible. Yttrium and titanium were not found in the same spatial position, which indicates, that titanium was already sequestered with carbon to form large carbides (see Figure 5) or that a dissolution of the Y-Ti-O precipitates occurred. From an energetic point of view, the dissolution of $Y_2Ti_2O_7$ or other complex phases, like $Y_2TiO_5$, is highly unlikely, due to their low Gibbs free energy of formation and the low solubility of yttrium in an austenitic matrix.
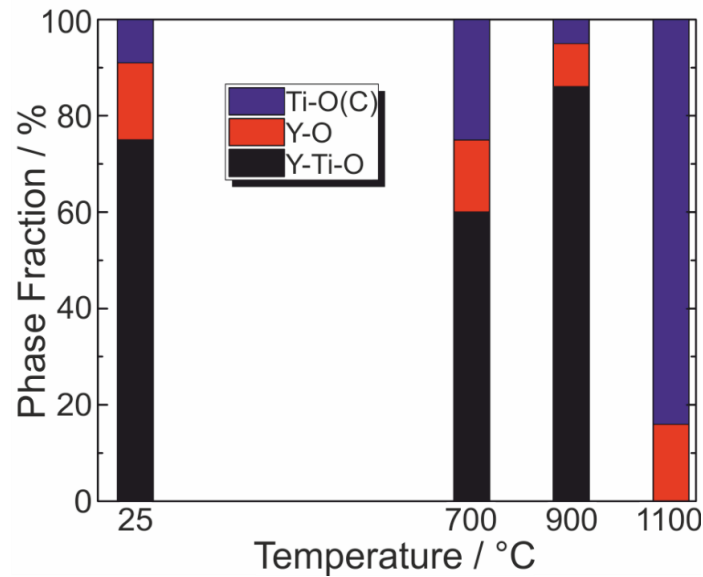


Figure 6: Change of the area phase fraction of precipitates after an annealing of 1500 hours at different temperatures.

Recently, Moghadasi et. al. [3] have quantified the influence of the oxygen partial pressure on the formation of precipitates in equilibrium state. They have shown, that a low oxygen partial pressure leads to a formation of $Y_2O_3$, a medium oxygen partial pressure supports the $Y_2TiO_5$ phase, while a higher oxygen partial pressure favors a formation of $Y_2Ti_2O_7$ and $Ti_2O_3$. Here, the overall oxygen content in material PCA-2 is relatively low (see Table 1), which let us conclude, that $Y_2O_3$ should be the most favorable phase in equilibrium state, but according to the analysis shown in Figure 6, this is only the case for the "1100 °C / 1500h" sample, while a lot of Y-Ti-O precipitates were found at all other temperatures and annealing times. A possible explanation could be an inhomogeneous distribution of oxygen, with a very low oxygen content available in sample "1100 °C / 1500h". Even though a similar ROI was investigated in all samples, the STEM EDS maps cover only a small region, which makes it difficult to derive comprehensive conclusions about the overall microstructure. Albeit no clear evidence of a phase transformation of the oxide precipitates has been found, a change of the size of the ODS particles was observed and is shown in Figure 7.
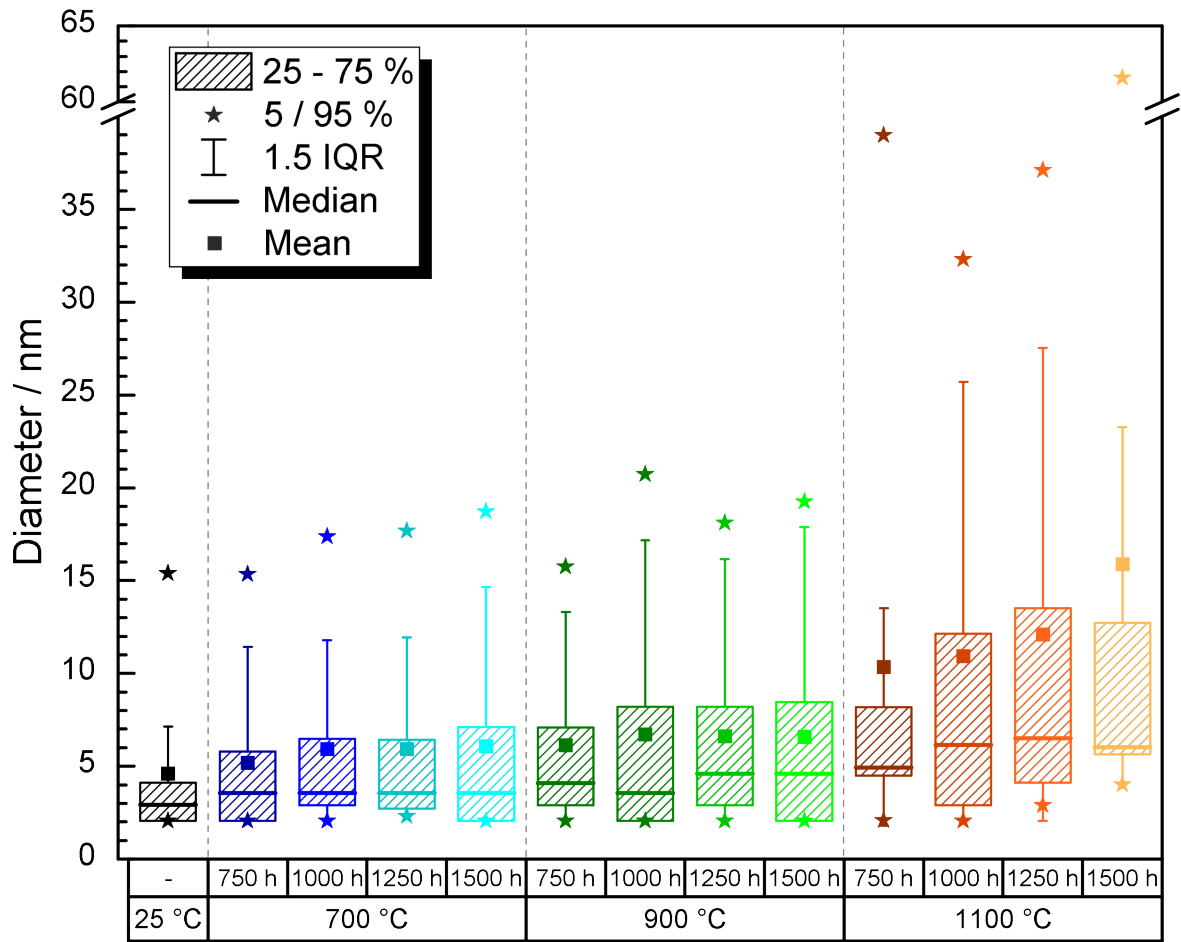
Figure 7: Statistical evaluation of the particle diameter of the TEM samples; the box frames the area betwee the 1st and the 3rd quantile, while the stars represent the 5 and 95 % percentile; whiskers show the smallest/ largest diameter inside the 1.5 times interquartile range. The axis of ordinates has a break between the values 40 and 60.

Figure 7 illustrates the collected data of the precipitate sizes for all annealing times and temperatures and the as-extruded condition as box-plots. The box itself represents the region between quartile 1 and quartile 3 (50 % of all determined diameters), while the 1.5 interquartile range (IQR) is indicated by whiskers. The 5% and 95 % percentile is displayed by stars. The difference between the mean and the median diameter can be used as an indicator for the skewness of the size distribution. While the smallest 5 % diameter size stays almost stable during all annealing temperatures and times (except 1100 °C / 1500 h), a stark increase of the 95 % threshold was determined for the 1100 °C samples. This means that the growth of larger precipitates seems to be directly connected to the annealing temperature and the diffusion of precipitate-forming elements. A comparison of the statistics obtained for the different annealing time at this temperature is indicative of a more inhomogeneous size distribution of precipitates: the IQR fluctuates significantly, 95 % threshold is strikingly increased, and the mean diameters increase stronger in size, while the median is more robust.

Table 3 shows that the number of precipitates decreases with an increasing annealing temperature. A general trend of an increased median and mean average precipitate size is also observed for increased annealing temperatures and annealing times. That indicates the dissolution of small precipitates in favor of the growth of other precipitates. To evaluate and compare the evolution of the spread of the distribution, the average sizes of the precipitates need to be taken into account. Thus, the quartile coefficients of dispersion (QCD) were determined, described as $QCD = (Q3 - Q1)/Median$ [15], and are displayed in

Table 3. According to this equation, a non-skewed normal curve is described by a QCD of 0.66. The QCD of 0.7 for the extruded material is close to the value of a normal curve, but it changes towards higher values (in a range

from 1.0 to 1.7) after a heat treatment was applied. This indicates that the skewness of the size distribution increases and that the bigger precipitates tend to grow even bigger. Another important finding is the decrease of the number of precipitates found in the ROI, which cannot be explained by deviations due to inhomogeneity in the microstructure, but are rather caused by the previously mentioned coarsening of precipitates on the expense of the dissolution of small precipitates.

Table 3: Summary of the collected data from TEM investigations.

| Temperature °C | Time h | Number - | Mean nm | Median nm | SD nm | Q1 nm | Q3 nm | QCD - |
|---|---|---|---|---|---|---|---|---|
| 25 °C | - | 1857 | 4.6 | 2.9 | 6.0 | 2.1 | 4.1 | 0.7 |
| 700 °C | 750 | 1637 | 5.2 | 3.6 | 5.1 | 2.1 | 5.8 | 1.1 |
| | 1000 | 1889 | 5.9 | 3.6 | 6.2 | 2.9 | 6.5 | 1.0 |
| | 1250 | 1246 | 5.9 | 3.6 | 6.0 | 2.7 | 6.4 | 1.0 |
| | 1500 | 1750 | 6.1 | 3.6 | 6.5 | 2.1 | 7.1 | 1.4 |
| 900 °C | 750 | 2535 | 6.1 | 4.1 | 5.4 | 2.9 | 7.1 | 1.0 |
| | 1000 | 1209 | 6.7 | 3.6 | 8.6 | 2.1 | 8.2 | 1.7 |
| | 1250 | 990 | 6.6 | 4.6 | 6.3 | 2.9 | 8.2 | 1.2 |
| | 1500 | 741 | 6.6 | 4.6 | 5.8 | 2.1 | 8.5 | 1.4 |
| 1100 °C | 750 | 287 | 10.3 | 4.9 | 15.0 | 4.5 | 8.2 | 0.7 |
| | 1000 | 368 | 10.9 | 6.2 | 17.4 | 2.9 | 12.1 | 1.5 |
| | 1250 | 514 | 12.1 | 6.5 | 18.2 | 4.1 | 13.5 | 1.4 |
| | 1500 | 228 | 15.9 | 6.0 | 26.3 | 5.6 | 12.7 | 1.2 |

SD: standard deviation; Q1: Quartile 1 (25 %); Q3: Quartile 3 (75 %); QCD: Quartile coefficient of dispersion

After the unexpected growth of precipitates was confirmed, it was interesting to investigate the connection of the growth of precipitates and the grain size. That was done by comparing the average values for each condition shown in Figure 8. The x-axis shows the annealing time and the y-axis represent the grain or precipitate size. The solid symbols represent the grain size and refer to the left y-axis, while the hollow symbols showing the precipitates mean diameter. Three general trends are highlighted with numbers 1 to 3 and colored green, yellow and blue, respectively. Trend 1 (green) shows the initial decrease of the grain size at 700 and 900 °C which then remains stable up to the here tested maximum annealing time of 1500 hours (see Figure 2). The error bars, which represents the standard deviation around the mean grain size diameter, is smaller than the displayed symbols. The decrease of the grain size was also reported and explained in other publications [8] TIM PAPER3. Trend 2 (yellow) shows the mean diameter of precipitates of the samples annealed at 700 and 900 °C. The statistically relevant information other than the mean value given in Figure 7 and Table 3 are not displayed here for better visibility. The mean diameter of precipitates is slightly higher than in the as-extruded condition, but no significant changes were found temperatures up to 900 °C. The comparison of trend 1 and 2 reveals, that after an initial change of size, the mean grain and precipitate diameter remain stable. However, trend 3 (blue) exhibits a different behavior. The grain and precipitate sizes have grown from 1.0 to 2.5 µm and 4.6 to 10.3 nm, respectively, after 750 hours at 1100 °C. The spread of the grain size is also an order of magnitude larger than the spread determined for all other temperatures. The aforementioned grain growth is found to be directly linked to the coarsening of precipitates, which exert a reduced Zener pinning pressure and enable the grains to grow. Due to the matter that the scale of both y-axis are linked, we can assume, that the grain and precipitates growth are linearly connected. Even though four average precipitate diameters were determined per temperature, a clear trend at of the type of growth of precipitates at 1100 °C is difficult to determine, especially considering the decreased numbers of precipitates found in the ROI, which lead to a decreased statistical significance. To get a clearer image of the coarsening process extended annealing times or even higher temperatures should be considered for future investigations.
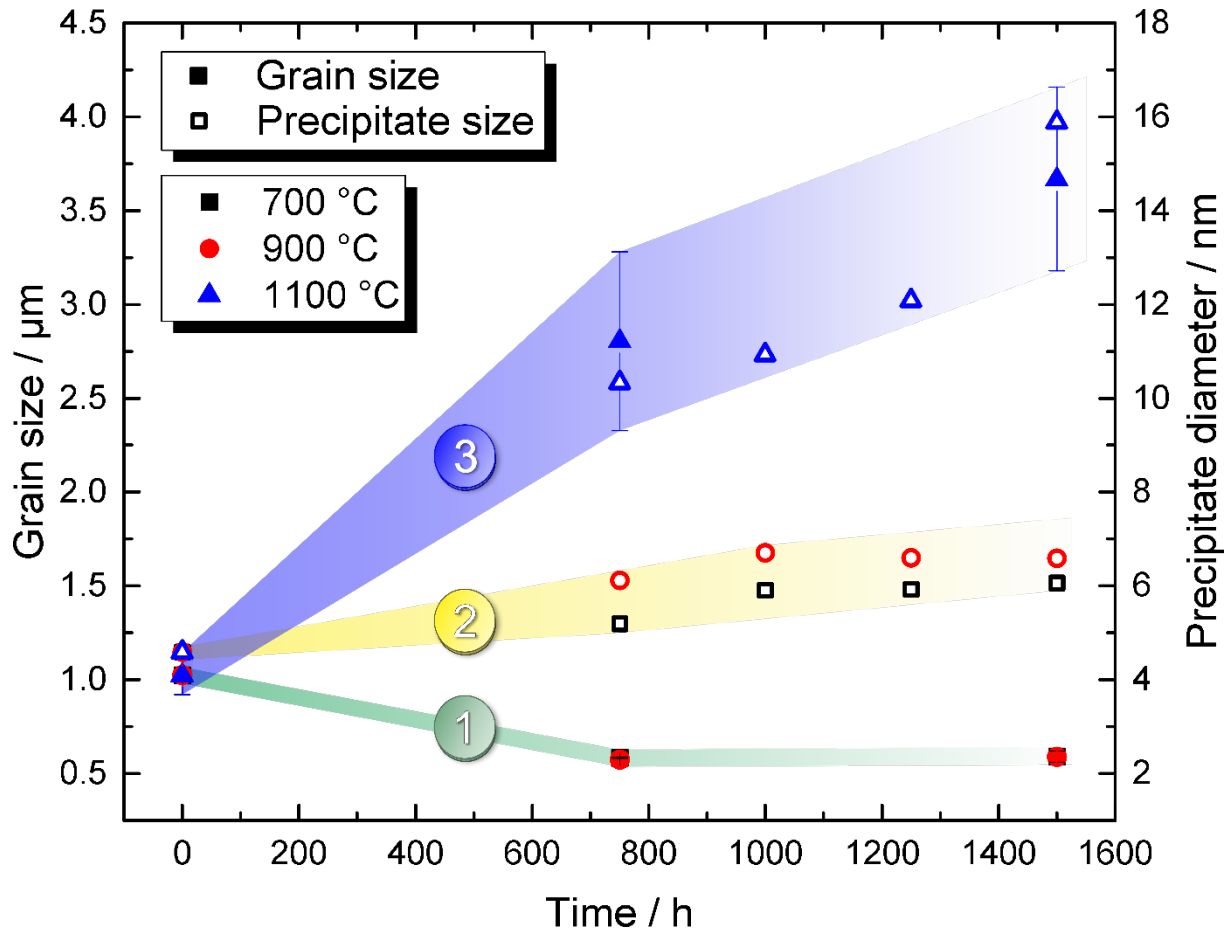
Figure 8:Grain size before and after a heat treatment at 700, 900, and 1100 °C between 750 and 1500 hours (full symbols refer to the left y-axis); Change of the average diameter of the precipitates after an annealing at different temperatures (open symbols refer to the right y-axis). Mean area grain sizes were analyzed by EBSD (see Figure 2); Mean diameters of precipitates were determined using multiple STEM EDS maps for each condition (see Figure 5 ). Error bars shown for the grain sizes represent the standard deviation between measurements of different areas of the same sample. The error bars are smaller than the displayed data point for the 700 and 900 °C samples. Error bars for the mean precipitate size are nor shown, due to the high spread of grain sizes (see Figure 7). The corresponding standard deviation is displayed in

Table 3.

Nevertheless, an approach to examine and understand the coarsening process with the present dataset was carried out. The mean precipitate diameter shown in Figure 8 and 8 of each annealing condition was used to calculate the activation energy for the coarsening process of the nano-precipitates. Coarsening of the precipitates in an alloy is controlled by diffusion of the essential elements of the precipitate and is driven by the reduction of the interface energy between precipitates and matrix material.  This mechanism is called Ostwald ripening and  is expressed by the following equation of the Lifshitz, Slyozof and Wagner (LSW) theory [2,6,16]:

*LSW theory*
$$d^3 - d_0^3 = k \cdot t \cdot \exp\left(\frac{-Q}{RT}\right) \qquad (4)$$

where $d$ and $d_0$ are the average diameter of the precipitates prior and after the annealing, respectively. The factor k is a material constant, t is the annealing time, Q the activation energy of the coarsening process, R the gas constant, and T the annealing temperature in Kelvin. Applying the natural logarithm to equation (4) and plotting the left part vs. 1/T let us estimate the activation energy, which is necessary for coarsening of the precipitates.
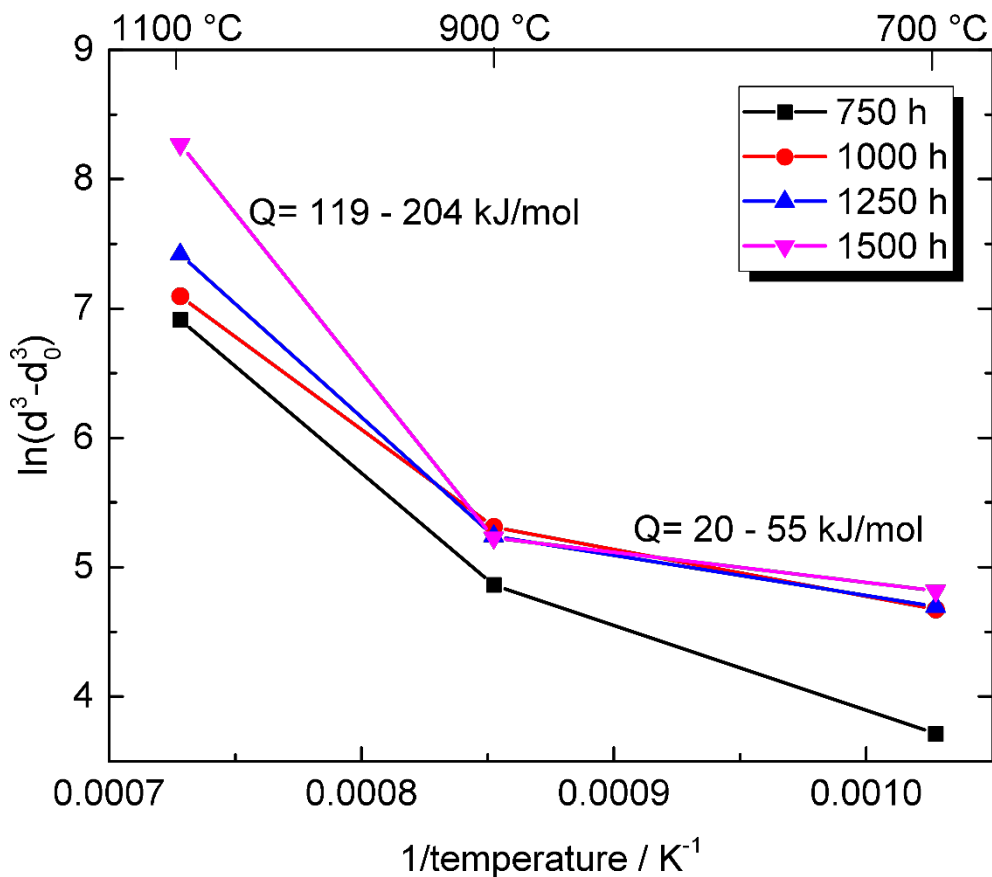
Figure 9: Arrhenius equation is showing the dependence of the mean particle size as a function of the inverse temperature for grain boundary diffusion [2]. Particles containing Y or Ti were used for the calculation of the activation energy Q.

The corresponding plot is illustrated in Figure 9. It shows the plots for the three annealing temperatures and 4 annealing times. In general, an increase of the calculated activation energy is visible at higher temperatures in comparison to the lower temperature regime (<900 °C). This indicates a shift of the coarsening mechanism, which was prior suggested by Kozikowski et al. [6]. However, due to the very long and cost-intensive annealing times, only three different times were applied, which makes it impossible to determine the exact temperature where the shift of the coarsening mechanism occurs. It can be safely assumed that the shift happens somewhere between 700 and 1100 °C, which is still lower, than the 1250 °C, which was found to be the transition temperature in prior research [6]. The calculated values of 20-55 kJ/mol as an activation energy for temperatures lower 900 °C restricts the diffusion of substitutional atoms and enables only the diffusion of interstitial elements, like oxygen or carbon [17]. The diffusion of the substitutional carbide or oxide forming elements is contingent on the availability of vacancies to jump to those nucleation sites, while the vacancies move in the opposite direction. The diffusion requires to overcome an element-depended energy threshold, which is provided as thermal energy during the annealing. The activation energy of the coarsening process of ODS precipitates between 900 and 1100 °C was determined to be between 119 and 204 kJ/mol. To understand and assess these obtained values, it is necessary to compare them to known activation energies of diffusion processes of ferritic and austenitic steels.

The activation energy for self-diffusion in α-Fe are calculated to be in a range of 251-299 kJ/mol [18–23]. However, the diffusion of large substitutional atoms like titanium and yttrium in ferritic steels is higher and calculated to be of around 400 kJ/mol [24]. Activation energies of yttrium and titanium in austenitic steels are more difficult to find in the literature, but are assumed to be even higher, considering the by magnitudes lower diffusion coefficients in austenitic steels in comparison to ferritic steels. The lower diffusion coefficient can be explained by the higher packing density of the face-centered cubic structure. The higher activation energy for self-diffusion of iron atoms in austenitic steels, which is about 284-337 kJ/mol, reflects that fact [20,25]. Here, the obtained activation energy values of 119 to 204 kJ/mol for the coarsening process of precipitates in the temperature range between 900 and 1100 °C are far off from the 535 kJ/mol, which were found by Kozikowski

et al. [6]. One possible explanation is the lack of intermediate points in the mentioned temperature range (see Figure 9). Under the assumption that the determined activation energy of around 50 kJ/mol for the 700-900 °C area continues and extends beyond the 900 °C limit, the inclination of the graph in the 900-1100 °C would become steeper, which would result in a higher activation energy. To reach values of around 400 kJ/mol, the shift would need to be in a temperature range between 1000 and 1050 °C, which is still much lower than the reported mechanism transition temperature of 1250 °C [6].

Another possible explanation could be that the growth of precipitates and the diffusion of substitutional atoms is supported by carbon [Reference-EXT-TIM]. Figure 10 shows a simplified scheme of the possible process for the purpose of a better visualization. Carbon easily diffuses even at relatively low temperatures and is often found around dislocations, due to the energetically preferable position, caused by exerted strain and stress field of the dislocation [26,27]. Dislocations are often pinned by ODS precipitates, which let us conclude, that carbon and the ODS precipitates can be found in spatial proximity in as-extruded condition, which is illustrated on the left-hand side of Figure 10: two ODS precipitates pin a carbon-enriched dislocation, while most of the other elements are dissolved in the matrix. A few smaller carbides have formed during the extrusion process and are shown on the bottom edge. Carbon tends to form carbides, especially $M_7C_3$ and $M_{23}C_6$ in this material, with M being a substitute for elements like Cr, W, and Mn. The precipitation process is driven by the reduction of the total free energy. The carbide nucleation requires the substitutional elements and also carbon atoms to diffuse towards each other and to nucleate at favorable sites. A dislocation is considered to be one of the favorable sites for nucleation and the necessary energy for diffusion is provided in form of thermal energy, during an annealing process. That means that the carbide forming elements diffuse towards a dislocation and form a carbide, while vacancies move in the opposite direction. Existing carbides also tend to grow, due to the same process. This state is displayed in the middle sketch "during annealing (I)" of Figure 10. We suggest that the formation of these fast growing carbides and the movement of vacancies may then supports the diffusion of other dissolved and substitutional elements like titanium or yttrium, by lowering their activation energy threshold by increasing the vacancy density in the proximity of the ODS precipitates. This process is illustrated in the image on the right-hand side of Figure 10, whereby the shown mechanisms "during annealing I" and "during annealing II" are not strictly limited to be consecutively, but also take place simultaneously.
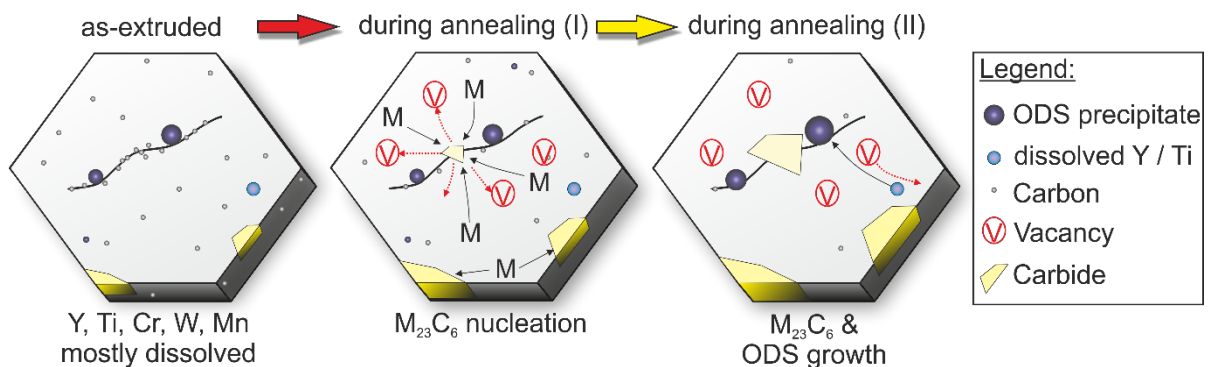


Figure 10: Scheme to explain the possible impact of carbon on the growth of ODS presipitates.

The impact of carbon on the mechanical properties of an austenitic ODS steel after annealing is shown in Figure 11. The hardness values are plotted on the y-axis against the annealing time at the three different temperatures. In as-extruded condition the hardness value of the rod in the ROI was determined to be around 385 HV 0.1. After a short annealing of 2 hours [Paper Tim], the hardness dropped to around 340 HV 0.1 for annealing temperatures of 700 and 900 °C and to 310 HV 0.1 for the 1100 °C sample. This hardness drop can be explained by a stress relaxation and recovery of the microstructure during initial states of annealing. After further annealing was carried out at 700 and 900 °C, no significant change in hardness was recorded. However, a slight increase of hardness after 1000 and 1250 hours was detected, which can only be explained by inhomogeneity in the material and the formation of carbides [Paper Tim]. However, the hardness didn't drop below the hardness level of the recovered microstructure (here shown after 2 hours of annealing). From a hardness point of view one could think, that the microstructure has not changed at all, but Figure 2Figure 8 demonstrated the change of the

grainsize and a slight increase of the average diameter of precipitates. We think that the mechanisms which increase the hardness, like the smaller grain size and the formation of carbides, counterbalance the softening mechanisms, like recovery of the microstructure, the growth of precipitates and the reduction of the number density of precipitates. This explains the larger hardness deviation in Figure 11 after an annealing at 700 and 900 °C was carried out. The long-term heat treatment at 1100 °C led to a decrease of the hardness, resulting in a value of around 250 HV 0.1 after 1500 hours. The increased grain and precipitate sizes are the main reason for the lower hardness.
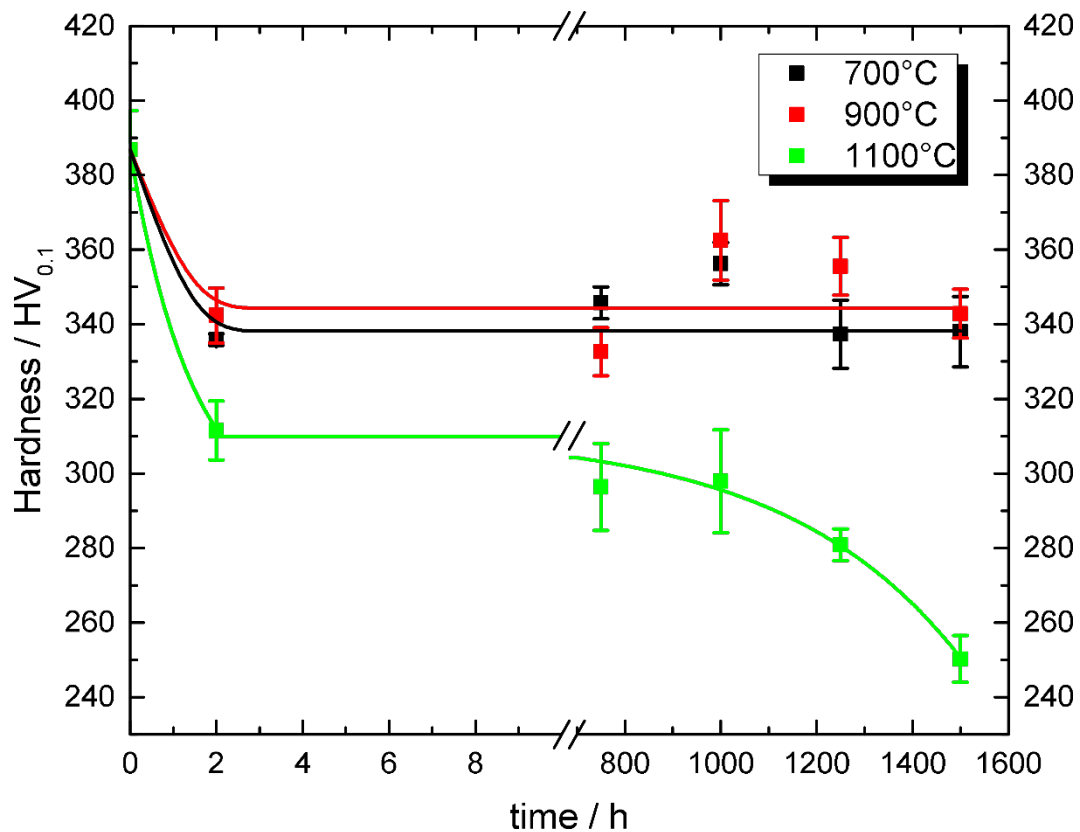


Figure 11: Hardness of the samples after annealing; measured in the ROI; each datapoint represents the avaerage hardness value of ten measurements; the error bars represent the minimum and maximum value.

## Conclusions

Long term annealing treatments at three different temperatures for up to 1500 hours were performed on extruded austenitic ODS steel. The change of the microstructure was investigated and linked to the presents of a carbon-rich process control agent. The conclusions are summarized here:

- A smaller grain size was measured after annealing treatments up to 900 °C, caused by recovery and recrystallization. The grain boundaries of newly formed grains were then pinned by nano precipitates. That means, that the Zener pinning pressure exerted by the nano-sized precipitates on the grain boundaries is higher than the driving force for grain growth at temperatures below 900 °C. The calculated activation energy for the growth of precipitates is below 50 kJ/mol, which is only enough for the diffusion of interstitial elements, like oxygen and carbon.
- Recovery, polygonisation and the reduction of stress during the heat treatments decreased the hardness by around 50 HV 0.1 (13 %) for annealing treatments at 700, 900 °C and by around 80 HV 0.1 (21%) for temperatures of 1100 °C.
- The hardness values of samples annealed up to 900 °C are somewhat stable, but longer heat treatments are needed to exclude the occurrence of a possibility compensation of hardening and softening

mechanisms indicated by the finding of larger carbides, which tend to increase the hardness of the material.

- The grain and precipitate sizes increased drastically during heat treatments at 1100 °C, which led to a significant hardness decreases. This unexpected finding was caused by the addition of a carbon-rich process control agent. We think, that carbon contributes to a reduction of the threshold energy for diffusion of elements like titanium and yttrium by forming carbides. That led to a strong growth of precipitates, which decreases the exerted grain boundary pinning force, and resulted in unprecedented grain growth at 1100 °C. The calculated activation energy between 900 and 1100 °C was determined to be in a range from 119 to 204 kJ/mol .

## Acknowledgements

## References

[1]     X. Mao, K.H. Oh, J. Jang, Mater. Charact. 117 (2016) 91–98.

[2]     F.J. Humphreys, M. Hatherly, Recrystallization and Related Annealing Phenomena, Repr. with, Pergamon, Oxford [u.a.], 1996.

[3]     M.A. Moghadasi, M. Nili-Ahmadabadi, F. Forghani, H.S. Kim, Sci. Rep. 6 (2016) 1–10.

[4]     M. Saber, W. Xu, L. Li, Y. Zhu, C.C. Koch, R.O. Scattergood, J. Nucl. Mater. 452 (2014) 223–229.

[5]     H. Sakasegawa, L. Chaffron, F. Legendre, L. Boulanger, T. Cozzika, M. Brocq, Y. de Carlan, J. Nucl. Mater. 384 (2009) 115–118.

[6]     Z. Oksiuta, P. Kozikowski, M. Lewandowska, M. Ohnuma, K. Suresh, K.J. Kurzydlowski, J. Mater. Sci. 48 (2013) 4620–4625.

[7]     J. Shen, H. Yang, Y. Li, S. Kano, Y. Matsukawa, Y. Satoh, H. Abe, J. Alloys Compd. 695 (2017) 1946–1955.

[8]     T. Gräning, M. Rieth, J. Hoffmann, A. Möslang, J. Nucl. Mater. 487 (2017) 348–361.

[9]     R. Agamennone, W. Blum, C. Gupta, J.K. Chakravartty, Acta Mater. 54 (2006) 3003–3014.

[10]    J. Schindelin, C.T. Rueden, M.C. Hiner, K.W. Eliceiri, Mol. Reprod. Dev. 82 518–29.

[11]    T. Kyu Kim, C. Hee Han, S. Hoon Kang, S. Noh, J. Jang, Curr. Nanosci. 10 (2014) 94–96.

[12]     a. Hirata, T. Fujita, Y.R. Wen, J.H. Schneibel, C.T. Liu, M.W. Chen, Nat. Mater. 10 (2011) 922–926.

[13]    A.J. London, S. Lozano-Perez, S. Santra, S. Amirthapandian, B.K. Panigrahi, C.S. Sundar, C.R.M. Grovenor, J. Phys. Conf. Ser. 522 (2014) 012028.

[14]    X. Mao, K.H. Oh, S.H. Kang, T.K. Kim, J. Jang, Acta Mater. 89 (2015) 141–152.

[15]    J.H. Zar, Biostatistical Analysis, Prentice-Hall, 1984.

[16]    H. Li, X. ping Song, Y. li Wang, G. liang Chen, J. Iron Steel Res. Int. 16 (2009) 81–86.

[17]    P. Thibaux, A. Métenier, C. Xhoffer, Metall. Mater. Trans. A 38 (2007) 1169–1176.

[18]    D.M. Reaman, H.O. Colijn, F. Yang, A.J. Hauser, W.R. Panero, Earth Planet. Sci. Lett. 349–350 (2012) 8–14.

[19]    D.W. James, G.M. Leak, Philos. Mag. 14 (1966) 701–713.

[20]    B. Zhang, AIP Adv. 4 (2014) 017128.

[21]    Y. Iijima, K. Kimura, K. Hirano, Acta Metall. 36 (1988) 2811–2820.

[22]    F.. Buffington, K. Hirano, M. Cohen, Acta Metall. 9 (1961) 434–439.

[23]    M. Lübbehusen, H. Mehrer, Acta Metall. Mater. 38 (1990) 283–292.

[24]    M.J. Alinger, G.R. Odette, D.T. Hoelzer, J. Nucl. Mater. 329–333 (2004) 382–386.

[25]    T. Heumann, R. Imm, J. Phys. Chem. Solids 29 (1968) 1613–1621.

[26]    R.G.A. Veiga, M. Perez, C.S. Becquart, C. Domain, S. Garruchet, Phys. Rev. B - Condens. Matter Mater. Phys. 82 (2010) 1–11.

[27]    O. Waseda, R.G. Veiga, J. Morthomas, P. Chantrenne, C.S. Becquart, F. Ribeiro, A. Jelea, H. Goldenstein, M. Perez, Scr. Mater. 129 (2017) 16–19.